

# InSb nanoparticles dispersion in Yb-filled $\text{Co}_4\text{Sb}_{12}$ improves the thermoelectric performance

Sanyukta Ghosh<sup>a</sup>, Sahil Tippireddy<sup>a</sup>, Gyan Shankar<sup>b</sup>, Anirudha Karati<sup>c</sup>, Gerda Rogl<sup>d</sup>, Peter Rogl<sup>d</sup>, Ernst Bauer<sup>e</sup>, Sai Rama Krishna Malladi<sup>f</sup>, B.S. Murty<sup>g</sup>, Satyam Suwas<sup>b</sup>, Ramesh Chandra Mallik<sup>a,\*</sup>

<sup>a</sup> Thermoelectric Materials and Devices Laboratory, Department of Physics, Indian Institute of Science, Bengaluru 560012, India

<sup>b</sup> Department of Materials Engineering, Indian Institute of Science, Bengaluru 560012, India

<sup>c</sup> Department of Chemistry, Indian Institute of Technology, Madras, Chennai 600036, India

<sup>d</sup> Institute of Materials Chemistry, University of Vienna, A-1090 Wien, Austria

<sup>e</sup> Institute of Solid State Physics, TU-Wien, A-1040 Wien, Austria

<sup>f</sup> Department of Materials Science and Metallurgical Engineering, Indian Institute of Technology, Hyderabad, Telangana 502285, India

<sup>g</sup> Department of Metallurgical and Materials Engineering, Indian Institute of Technology, Madras, Chennai 600036, India

## ARTICLE INFO

### Article history:

Received 16 February 2021

Received in revised form 8 May 2021

Accepted 22 May 2021

Available online 25 May 2021

### Keywords:

Thermoelectrics

Nanocomposite

EBS

Lattice thermal conductivity

Indium antimonide

## ABSTRACT

Out of several methods, one of the most explored strategies to decrease the lattice thermal conductivity of  $\text{Co}_4\text{Sb}_{12}$ -based materials are either filling suitable electropositive elements into the voids or the formation of nanocomposites. These two approaches were combined in this work by filling Yb into the void of  $\text{Co}_4\text{Sb}_{12}$  and preparing nanocomposites of  $\text{Yb}_{0.2}\text{Co}_4\text{Sb}_{12}$  and InSb according to the formula  $(\text{InSb})_x + \text{Yb}_{0.2}\text{Co}_4\text{Sb}_{12}$  (where  $x = 0.1, 0.2, 0.3, 0.4$ ), via ball-milling and spark plasma sintering.  $\text{Yb}_2\text{O}_3$  and  $\text{CoSb}_2$  as impurity phases were found at the grain boundaries. EBSD and TEM micrographs showed nanocrystalline InSb phase (20–200 nm) dispersed in the matrix grains. The charge transfer from Yb filler with an oxidation state of +3 to  $\text{Co}_4\text{Sb}_{12}$  yielded a low electrical resistivity ( $\rho$ ) of the matrix. An increase in  $\rho$  and Seebeck coefficient ( $S$ ) in the composites with  $x = 0.1$  and  $0.3$  occurred due to the higher amount of oxide impurities in these two samples and the scattering of charge carriers at the interfaces induced by the secondary phases. The other two composites with  $x = 0.2$  and  $0.4$  exhibited  $\rho(T)$  and  $S(T)$  similar to the  $\text{Yb}_{0.2}\text{Co}_4\text{Sb}_{12}$  matrix. The dispersion of the InSb and  $\text{Yb}_2\text{O}_3$  phases at the grain boundaries combined with the anharmonicity introduced by the fillers (Yb) in the voids enhanced the scattering of phonons within a broad wavelength range and reduced the lattice thermal conductivity significantly. Hence, a highest  $zT$  of  $\sim 1.2$  at 773 K with a thermoelectric efficiency of 8.89% and 8.28% (423–773 K) were obtained for  $(\text{InSb})_{0.1} + \text{Yb}_{0.2}\text{Co}_4\text{Sb}_{12}$  and  $(\text{InSb})_{0.2} + \text{Yb}_{0.2}\text{Co}_4\text{Sb}_{12}$  nanocomposites, respectively.

© 2021 Elsevier B.V. All rights reserved.

## 1. Introduction

Thermoelectricity provides an alternative source for renewable energy by converting heat into electricity. The efficiency of a thermoelectric material is dependent on the dimensionless quantity called the figure of merit  $zT = S^2T/\rho\kappa$ , where  $S$  is the Seebeck coefficient,  $\rho$  is the electrical resistivity,  $\kappa$  is the thermal conductivity comprising two parts: the electronic contribution ( $\kappa_e$ ) and the lattice contribution ( $\kappa_L$ ) ( $\kappa = \kappa_e + \kappa_L$ ); and  $T$  is the absolute temperature.  $zT$  can be increased by enhancing  $S$  and decreasing  $\rho$  and  $\kappa$ . The limited

efficiency of the thermoelectric devices stems from the inter-relation of these three parameters, which makes it difficult and challenging to decouple and optimize them independently.

$\text{Co}_4\text{Sb}_{12}$ -based skutterudite materials are highly efficient mid-temperature (300–800 K) thermoelectric materials with high charge carrier mobilities [1] and a reasonable bandgap ( $\sim 0.2$  eV) [2–5]. The symmetric crystal structure of  $\text{Co}_4\text{Sb}_{12}$  (body-centered cubic (bcc), space group  $\text{Im}\bar{3}$ ) produces high band degeneracy [6], which is helpful for high thermoelectric efficiency. But, the high lattice thermal conductivity ( $\sim 7.5$  W/m-K at room temperature) due to a strong Co-Sb covalent bonding results in a very low  $zT$  value (0.05 at 723 K) and a low thermoelectric efficiency [7]. Slack et al. [8] proposed the “phonon-glass-electron-crystal” concept, which suggests filling voids at the 2a Wyckoff position in the  $\text{Co}_4\text{Sb}_{12}$  crystal structure by electropositive elements to

\* Corresponding author.

E-mail address: [rcmallik@iisc.ac.in](mailto:rcmallik@iisc.ac.in) (R.C. Mallik).

decrease the lattice contribution of thermal conductivity. Fillers, being loosely bound to Sb atoms, rattle inside the large voids with large thermal parameters, effectively reducing the lattice thermal conductivity via strong phonon scattering due to the resonant interaction between guest atoms and lattice phonons [8]. The electropositive fillers also provide their valence electrons to the conduction band, transforming  $\text{Co}_4\text{Sb}_{12}$  into heavily doped n-type materials. Thus, the void filling of  $\text{Co}_4\text{Sb}_{12}$  can optimize the electrical resistivity and thermal conductivity, having a minimal negative effect on the Seebeck coefficient [9–12]. Another strategy to decrease the lattice thermal conductivity is the dispersion of nanocrystalline secondary phases in the bulk  $\text{Co}_4\text{Sb}_{12}$  matrix [13–17]. The interfaces, induced by such nano-sized secondary phases, can scatter phonons of comparable wavelengths and lower  $\kappa_L$ . The reported nano-sized secondary phases in bulk  $\text{Co}_4\text{Sb}_{12}$  are metals, oxides, intermetallics, borides, tellurides, nitrides, silicides, antimonides, 2-dimensional, and 3-dimensional (nanotubes or buckyballs) carbon phases [18].

In this work, these two approaches were combined to reduce the lattice contribution of the thermal conductivity to the minimum possible value ( $\sim 0.5$  W/m-K [19]). Electropositive Yb was selected as filler because Yb with a probable oxidation state of +2 and +3 is expected to donate charge carriers and reduce the electrical resistivity of  $\text{Co}_4\text{Sb}_{12}$  [20–22]. Small and heavyweight Yb can also scatter the long-wavelength phonons and reduce the lattice thermal conductivity. Consequently, a  $zT \sim 1$  between 600 K and 800 K was reported for Yb-filled  $\text{Co}_4\text{Sb}_{12}$  [20–22]. InSb was selected as a nano-sized additive phase to further decrease the lattice thermal conductivity by enhanced interface scattering of the phonons with a mean free path comparable to the grain size of InSb [23–27]. In this work, the thermoelectric properties of  $\text{Yb}_{0.2}\text{Co}_4\text{Sb}_{12}$  and InSb nanocomposites were investigated in detail. The electrical resistivity and Seebeck coefficient were influenced by the InSb inclusion phase and other impurity phases, such as  $\text{Yb}_2\text{O}_3$  and  $\text{CoSb}_2$ , present in the composites. A significant reduction in  $\kappa_L$  led to a high  $zT \sim 1.2$  at 773 K for  $(\text{InSb})_{0.1} + \text{Yb}_{0.2}\text{Co}_4\text{Sb}_{12}$  and  $(\text{InSb})_{0.2} + \text{Yb}_{0.2}\text{Co}_4\text{Sb}_{12}$  composites.

## 2. Experimental procedure

### 2.1. Synthesis

$\text{Yb}_{0.4}\text{Co}_4\text{Sb}_{12}$  was synthesized using the traditional melting-quenching-annealing technique. Previous studies reported a filling fraction limit of  $\sim 0.2$ – $0.3$  for Yb in  $\text{Co}_4\text{Sb}_{12}$  voids, both theoretically [28–30] and experimentally [20] using the conventional melting-quenching-annealing synthesis method. An Yb content higher than the reported filling fraction limit was taken at the time of synthesis to compensate for its loss. Highly pure Cobalt (99.999%), Antimony (99.999%), and Ytterbium (99.999%) were sealed in carbon-coated quartz ampoules under a dynamic vacuum of  $10^{-4}$  mbar and induction melted for 10 min at 1130 K, afterward quenched to room temperature using regular water. The samples were then annealed for 168 h at 973 K. The obtained ingots were powdered with an agate mortar and pestle. The characterization results revealed a 0.2 filling fraction of Yb in  $\text{Co}_4\text{Sb}_{12}$ , and therefore, the composition of the matrix is referred to as  $\text{Yb}_{0.2}\text{Co}_4\text{Sb}_{12}$  in the entire manuscript. Nano-powder of InSb was produced via ball-milling of commercially available InSb (99.99%) powder for 5 h at 400 rpm. Then it was uniformly mixed with  $\text{Yb}_{0.2}\text{Co}_4\text{Sb}_{12}$  by ball-milling at 100 rpm for 40 min following the formula of  $(\text{InSb})_x + \text{Yb}_{0.2}\text{Co}_4\text{Sb}_{12}$  ( $x = 0.1, 0.2, 0.3, 0.4$ ), which corresponds to 1.37, 2.73, 4.10, and 5.46 wt% of InSb in  $\text{Yb}_{0.2}\text{Co}_4\text{Sb}_{12}$  respectively. The nanocomposite powder was consolidated using a Dr. Sinter SPS-625 spark plasma sintering (SPS) device at 873 K for 5 mins by applying a pressure of 50 MPa at a vacuum of 0.5 mbar. High-density pellets ( $\sim 98 \pm 1\%$  of the theoretical density) were obtained and cut for thermoelectric properties measurements. The electrical resistivity and Seebeck coefficient were measured using rectangular ( $12 \times 2 \times 2$  mm<sup>3</sup>) cuboids, and thermal

conductivity was measured using cylindrical discs (6 mm diameter  $\times$  1 mm thickness).

### 2.2. Characterization

The phase formation of the powder samples was checked at room temperature using a Rigaku Smartlab X-ray diffraction (XRD) system equipped with a Cu K $\alpha$  radiation source of 1.5418 Å wavelength. The Rietveld refinement of the experimental XRD pattern was performed employing the FullProf software and the lattice parameter of the composites was determined. The microstructure was acquired with JEOL JXA-8530F electron probe microanalyses (EPMA), and the compositional analyses of the composites were performed using wavelength dispersive spectroscopy (WDS) and energy dispersive spectroscopy (EDS) techniques, attached with the EPMA instrument. In the matrix, the distribution of InSb inclusions and their grain size were observed with an FEI Helios NanoLab Dual-beam electron back-scattered diffraction (EBSD) system with a step size of 50 nm, and transmission electron microscopy (TEM) [JEM-2100(HR)] equipped with a LaB<sub>6</sub> source. Data analysis of the EBSD scan relied on the TSL OIM 8.1 software. GATAN Digital micrograph software was used to analyze TEM data. A Kratos Axis Ultra system having an Al K $\alpha$  source supplied X-ray photoelectron spectra (XPS). The Raman active modes of the composites were recorded in a LabRAM HR (UV) system with a laser of 532 nm wavelength at room temperature. The carrier concentration at room temperature was obtained from Hall measurements. The differential and four-probe methods were employed to measure the Seebeck coefficient (measurement error 7%) and the electrical resistivity (measurement error 10%) respectively in the temperature range of 423–773 K using a LINSEIS LSR-3 system. The laser flash method was used to measure the thermal conductivity ( $\kappa$ ) via the equation:  $\kappa = DC_p d$ , where  $d$  is the density of the samples,  $D$  is the thermal diffusivity and  $C_p$  is the specific heat by a Flashline 3000, ANTER system (measurement error 6%) in the temperature range of 423–773 K.  $C_p$  was measured using a TA instrument DSC 25. Finally, the thermoelectric  $zT$  of the materials (with an error of  $\sim 15\%$ ) was calculated with the values of  $S$ ,  $\rho$  and  $\kappa$ .

## 3. Results and discussion

### 3.1. Powder X-ray diffraction (PXRD)

The powder XRD patterns of  $(\text{InSb})_x + \text{Yb}_{0.2}\text{Co}_4\text{Sb}_{12}$  ( $x = 0, 0.1, 0.2, 0.3, 0.4$ ) composites are plotted in Fig. 1(a), indexed with the corresponding (hkl) crystallographic planes of pure  $\text{Co}_4\text{Sb}_{12}$  [ICSD # 41620]. All the composites were crystalline, established from the sharp XRD peaks. The amount of InSb inclusion phase ( $\leq 5.46$  wt%) in the composites was below the instrumental detection limit. Hence, no peak corresponding to InSb secondary phases was noticed in the XRD pattern. The lattice parameter of the composites was evaluated from the Rietveld refinement of the XRD patterns using the FULLPROF program [31]. The refined pattern of  $(\text{InSb})_{0.1} + \text{Yb}_{0.2}\text{Co}_4\text{Sb}_{12}$  is displayed in Fig. 1(b), and the refined patterns of other samples are provided in Supplementary Material, Section 1. The lattice parameter of the composites is in the range of  $\sim 9.050$  Å (Table 1). This lattice parameter value is higher than that of pure  $\text{Co}_4\text{Sb}_{12}$  ( $\sim 9.035$  Å) [7] because filling Yb in the voids of the  $\text{Co}_4\text{Sb}_{12}$  structure expanded the unit cell, as also reported in previous studies [21,32]. Further addition of InSb in  $\text{Yb}_{0.2}\text{Co}_4\text{Sb}_{12}$  did not change the lattice parameter because it was in the samples as a separate phase.

### 3.2. Microstructure and phase characterization

#### 3.2.1. Electron probe micro analyses (EPMA)

Fig. 2(a–e) displays the backscattered electron (BSE) micrographs of the polished surface of the composites  $(\text{InSb})_x + \text{Yb}_{0.2}\text{Co}_4\text{Sb}_{12}$

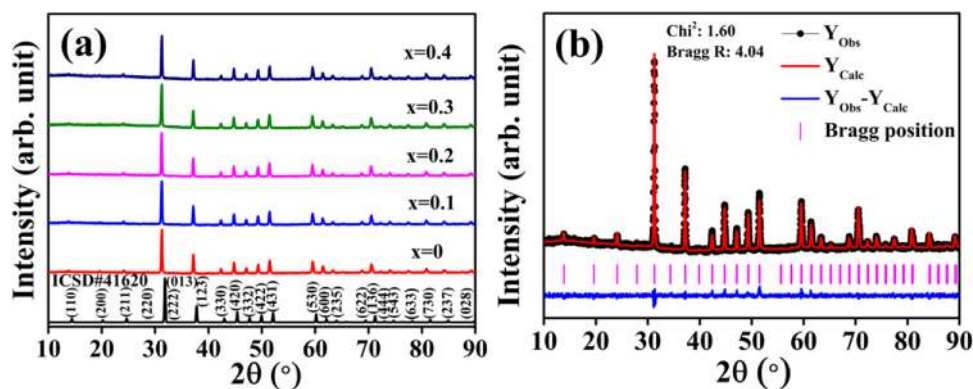


Fig. 1. (a) Powder XRD patterns of  $(\text{InSb})_x + \text{Yb}_{0.2}\text{Co}_4\text{Sb}_{12}$  ( $x = 0, 0.1, 0.2, 0.3, 0.4$ ), (b) Rietveld refinement of XRD pattern of  $(\text{InSb})_{0.1} + \text{Yb}_{0.2}\text{Co}_4\text{Sb}_{12}$ .

Table 1

Nominal composition, actual composition determined using WDS-EPMA (normalized to 12 atoms of Sb), lattice parameter, and relative density of the composites.

Nominal composition	Composition determined via WDS-EPMA		Lattice parameter (Å)	Relative density (%)
	Matrix phase	Secondary phase (vol%)		
$\text{Yb}_{0.4}\text{Co}_4\text{Sb}_{12}$	$\text{Yb}_{0.18}\text{Co}_{3.93}\text{Sb}_{12}$	$\text{CoSb}_2$ (2.69%), $\text{Yb}_2\text{O}_3$ (0.97%)	9.049(3)	99.5
$(\text{InSb})_{0.1} + \text{Yb}_{0.4}\text{Co}_4\text{Sb}_{12}$	$\text{Yb}_{0.18}\text{Co}_{3.96}\text{Sb}_{12}$	$\text{CoSb}_2$ (3.26%), $\text{Yb}_2\text{O}_3$ (1.18%)	9.051(1)	98.6
$(\text{InSb})_{0.2} + \text{Yb}_{0.4}\text{Co}_4\text{Sb}_{12}$	$\text{Yb}_{0.19}\text{Co}_{3.98}\text{Sb}_{12}$	$\text{CoSb}_2$ (2.32%), $\text{Yb}_2\text{O}_3$ (0.89%), InSb	9.052(2)	99.9
$(\text{InSb})_{0.3} + \text{Yb}_{0.4}\text{Co}_4\text{Sb}_{12}$	$\text{Yb}_{0.19}\text{Co}_{4.02}\text{Sb}_{12}$	$\text{CoSb}_2$ (2.04%), $\text{Yb}_2\text{O}_3$ (1.21%), InSb	9.053(2)	97.9
$(\text{InSb})_{0.4} + \text{Yb}_{0.4}\text{Co}_4\text{Sb}_{12}$	$\text{Yb}_{0.19}\text{Co}_{3.89}\text{Sb}_{12}$	$\text{CoSb}_2$ (2.17%), $\text{Yb}_2\text{O}_3$ (0.85%), InSb	9.053(8)	97.8

( $x = 0, 0.1, 0.2, 0.3, 0.4$ ). The micrographs revealed a dense morphology of the composites. Apart from the main grey phase of  $\text{Co}_4\text{Sb}_{12}$ , two additional secondary phases (dark grey and white colored region) were detected in the BSE micrographs. The dark grey region belongs to the  $\text{CoSb}_2$  phase. The formation of  $\text{CoSb}_2$  is quite common during the synthesis of filled  $\text{Co}_4\text{Sb}_{12}$  and is also reported in previous studies [21,33]. The white-colored phase observed in Fig. 2 was attributed to  $\text{Yb}_2\text{O}_3$ . Ryll et al. [21] also reported the formation of a  $\text{Yb}_2\text{O}_3$  secondary phase in  $\text{Yb}_x\text{Co}_4\text{Sb}_{12}$ . InSb, likely due to its low volume content ( $\approx 1.37$  wt%), was not detected in the BSE micrographs of the  $x = 0.1$  composite. For a higher content of InSb ( $x > 0.1$ ), both the InSb and  $\text{Yb}_2\text{O}_3$  secondary phases were found segregated at the grain boundary. The EDS spectra were taken at the white-colored region of the composite with  $x = 0.3$ , shown in Fig. 2(e). In and Sb elements were also detected in the white-colored (oxide phase) region with Yb and O in the EDS spectra. The composition of the constituent phases of the composites was evaluated using WDS and is given in Table 1. The filling fraction limit of Yb from WDS is around  $\sim 0.2$  in the samples, which is in good agreement with previous studies [20,28–30]. The surplus Yb formed the secondary phase of  $\text{Yb}_2\text{O}_3$ . The vol% of the secondary phases were determined from the phase contrast in the BSE microstructure using ImageJ software and are listed in Table 1. It approximates the volume fraction of the different phases as we investigate a tiny region of the samples. Supplemental Fig. S2(a–g) displays the elemental map of the  $(\text{InSb})_{0.4} + \text{Yb}_{0.2}\text{Co}_4\text{Sb}_{12}$  composite, using WDS-EPMA. The grey colored region of the micrograph showed the homogeneous spreading of Co and Sb, together with a small amount of Yb. The white-colored region was mainly Yb and O rich with a slightly lower concentration of In and Sb ( $\sim 15$  at%), and hence the white region is the combination of InSb and  $\text{Yb}_2\text{O}_3$  phases. This white colored phase was also found at the grain boundaries of the composites from the elemental mapping.

### 3.2.2. Electron back scatter diffraction (EBSD)

Fig. 3(a–c) shows the EBSD phase map of the  $(\text{InSb})_{0.4} + \text{Yb}_{0.2}\text{Co}_4\text{Sb}_{12}$  composite revealing the distribution of different phases and their grain size. The matrix  $\text{Yb}_{0.2}\text{Co}_4\text{Sb}_{12}$  exhibits a bimodal distribution of grains, where the bigger grains are 15–25  $\mu\text{m}$  in size,

as observed in Fig. 3(a). Some nanocrystalline matrix grains in the size of 200–400 nm were found distributed along with nanocrystalline InSb grains [Fig. 3(c)]. The distribution of the nanocrystalline InSb phase, represented in green color in the matrix, was observed from the magnified portion of the matrix in Fig. 3(b). The agglomeration of InSb nanoparticles resulted in some large grains of InSb (5–8  $\mu\text{m}$ ) in the phase map.

Supplemental Fig. S3 (a–d) exhibits the inverse pole figure (IPF) map of the constituting phases and their normal direction (ND) IPF of the  $(\text{InSb})_{0.4} + \text{Yb}_{0.2}\text{Co}_4\text{Sb}_{12}$  composite. The orientation of the matrix grains was along the directions [013] and [223], parallel to the SPS axis. InSb shows a spread of orientation between the [104] and [115] directions, parallel to the SPS axis. The orientation of the crystals plays an essential role in electrical and thermal transport. It was observed that the crystal orientation along the close-packed direction leads to higher thermal conductivity values, which for bcc structures is the [111] direction and for fcc structure are the [101], [110], and [011] directions [34]. Since the crystal orientation of both, the matrix and InSb phase, is not in the close-packed direction, it will contribute towards a lower thermal conductivity value of the composites.

### 3.2.3. Transmission electron microscopy (TEM)

The distribution of nanoparticles was also investigated by TEM. The bright-field micrographs, displayed in Fig. 4(a and b), confirmed the existence of nanocrystalline particles and their accumulation in the composite. High-resolution micrographs captured from the same area show nanocrystalline grains of InSb of size 20–200 nm. The grains of the matrix phase were also detected in TEM micrographs.

The Fast Fourier Transform (FFT), obtained via the DigitalMicrograph software from the HRTEM micrographs, measuring the lattice spacing from Inverse Fast Fourier Transform (IFFT) along with energy dispersive X-ray spectrometry (EDX) analysis helped to detect the phases present in the sample. The FFT obtained from the matrix phase, and the InSb phase confirmed the bcc (region 2) and fcc (region 1 and 3) crystal structure, respectively. Li et al. showed a substantial reduction in lattice thermal conductivity of  $\text{In}_x\text{Ce}_y\text{Co}_4\text{Sb}_{12}$ , attributable to the strong scattering of phonons at the InSb interfaces of size 10–80 nm [25]. Similarly, Gharleghi et al. observed effective scattering of phonons at the InSb

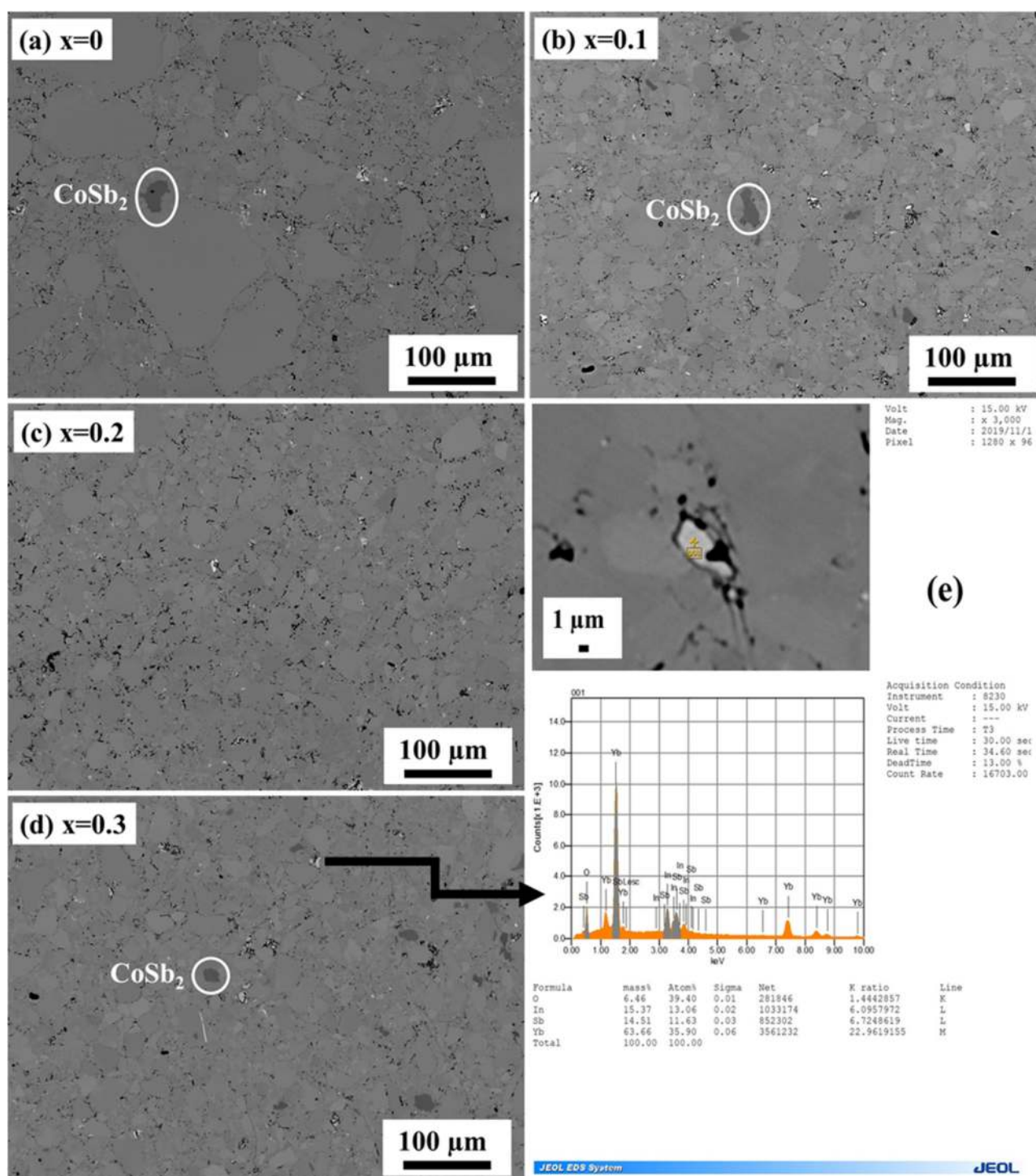


**Fig. 2.** EPMA micrographs of  $(\text{InSb})_x + \text{Yb}_{0.2}\text{Co}_4\text{Sb}_{12}$ , for (a)  $x=0$ , (b)  $x=0.1$ , (c)  $x=0.2$ , (d)  $x=0.3$ , (e) EDS spectra taken at white colored secondary phase (pointed out with an arrow) of  $x=0.3$  sample.

grains of size 30–50 nm [26]. Hence, these nano-sized InSb grains in the bulk matrix of  $\text{Yb}_{0.2}\text{Co}_4\text{Sb}_{12}$  with  $\text{Yb}_2\text{O}_3$  and  $\text{CoSb}_2$  secondary phases are expected to scatter phonons of a wide wavelength range, which will help to improve the thermoelectric figure of merit by reducing the lattice part of thermal conductivity.

### 3.3. Raman spectroscopy

Fig. 5 displays the Raman spectra of the  $x=0$  and 0.4 composites. A Silicon reference (Raman active peak at  $520.5\text{ cm}^{-1}$ ) was used to

calibrate the spectra. The spectra peaks were fitted using the Gaussian and Lorentzian profiles, and the peak positions are listed in Table 2. The first-order Raman modes of  $\text{Co}_4\text{Sb}_{12}$ , as predicted from group theory, are  $2A_g + 2E_g + 4F_g$  [23,36,37]. The majority of the peaks of the spectra correspond to the vibration of Sb in the  $\text{Sb}_4$  ring. The elongation of the large and the short Sb-Sb bond generated two  $A_g$  peaks at  $149\text{ cm}^{-1}$  and  $182\text{ cm}^{-1}$ , respectively [23,38]. An exact square  $\text{Sb}_4$  ring will generate one  $A_g$  peak rather than two peaks. The peak at  $132\text{ cm}^{-1}$  is assigned to the  $E_g$  mode of Sb, and the peaks at  $83\text{ cm}^{-1}$ ,  $106\text{ cm}^{-1}$ , and  $175\text{ cm}^{-1}$  are assigned to the  $F_g$  mode. One

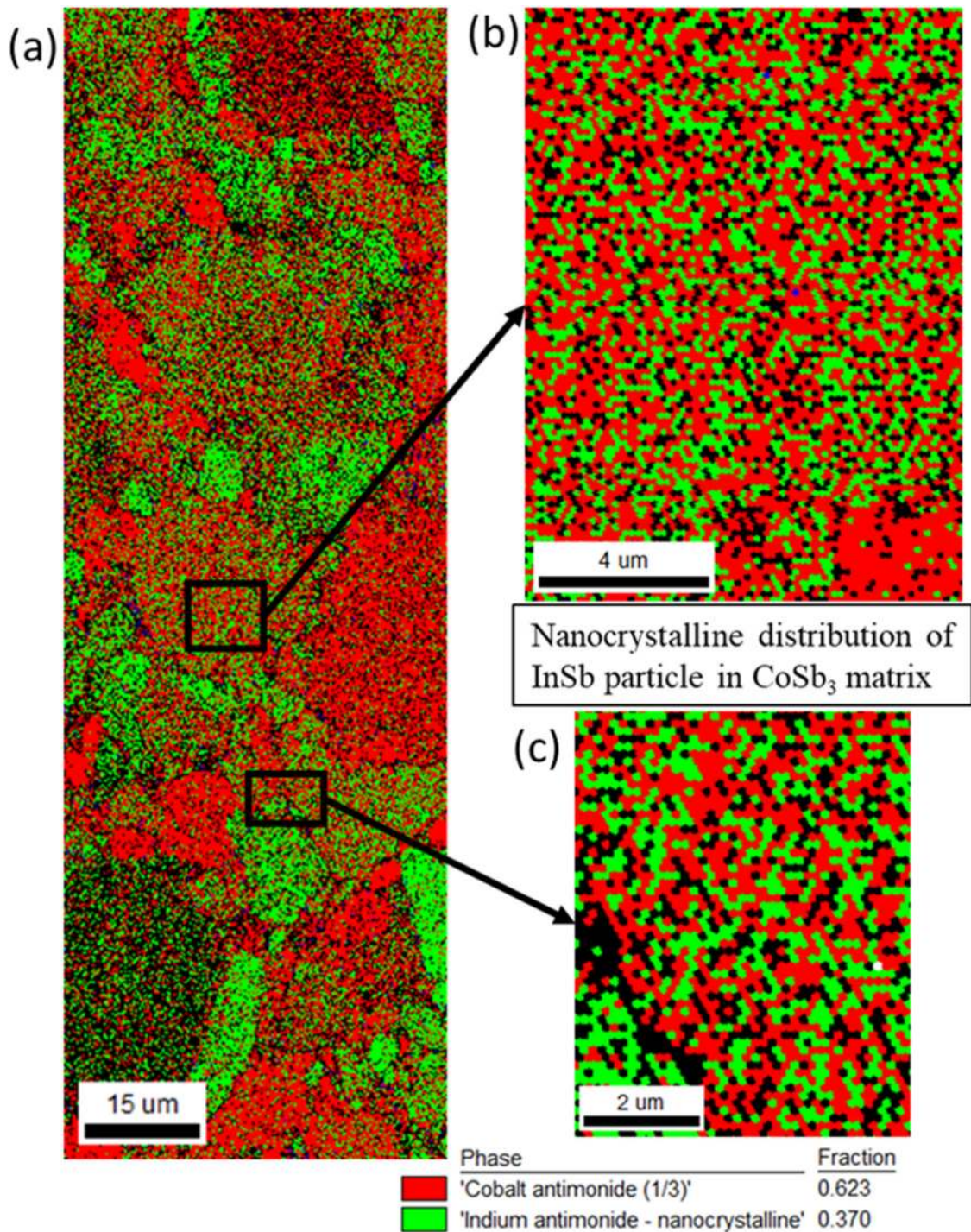


**Fig. 3.** EBSD phase map of  $(\text{InSb})_{0.4} + \text{Yb}_{0.2}\text{Co}_4\text{Sb}_{12}$  showing (a) grain size, shape, and the distribution of each phase through different colors, (b), and (c) a magnified area reveals the nanocrystalline distribution of different phases.

additional Raman active mode  $F_u$  at  $60 \text{ cm}^{-1}$  was detected, which was also observed in filled skutterudite by Rogl et al. [36], and Lu et al. [39], originating from the vibration of the fillers in the voids, although a peak at the same position ( $60 \text{ cm}^{-1}$ ) was also observed by Nolas et al. in case of pure  $\text{Co}_4\text{Sb}_{12}$ .

The peak at  $121 \text{ cm}^{-1}$  likely stems from the  $\text{CoSb}_2$  secondary phase [23]. The difference in intensity of different modes of the two composites mainly originated from the inhomogeneity of the samples and the presence of multiple phases. A softening of phonon vibrations in the composites, evident from the shift of Raman active modes towards the lower wavenumber, compared to that of pure

$\text{Co}_4\text{Sb}_{12}$ , was due to the Yb filling in the voids [36,38]. This happens because rattling of Yb in the void distorts the  $\text{Sb}_4$  ring by stretching the Sb-Sb bond and decreasing the force constant. The anharmonicity created by the distorted  $\text{Sb}_4$  ring leads to a lower lattice thermal conductivity.

### 3.4. Thermoelectric properties

#### 3.4.1. Electrical resistivity ( $\rho$ )

An increase in  $\rho(T)$  with temperature was observed for the composites, demonstrating a degenerate semiconductor behavior

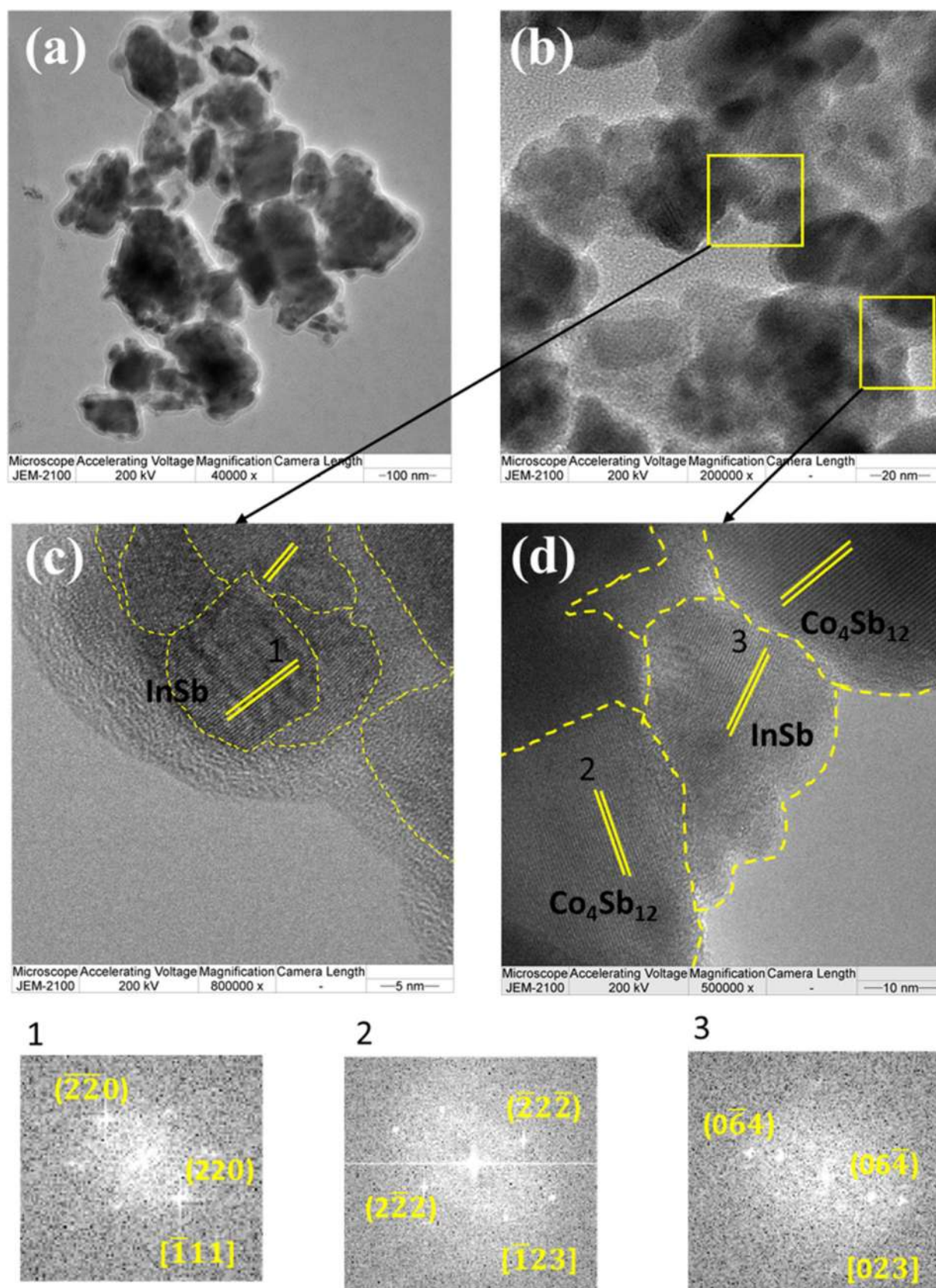


**Fig. 4.** (a) and (b) Bright-field TEM micrograph showing the agglomerated nanoparticles, (c) and (d) high-resolution TEM micrographs from the squared area showing the dispersion of  $\text{Yb}_{0.2}\text{Co}_4\text{Sb}_{12}$  and InSb phases, and fast Fourier transform generated from the marked areas 1, 2 and 3 of the  $(\text{InSb})_{0.1} + \text{Yb}_{0.2}\text{Co}_4\text{Sb}_{12}$  composite.

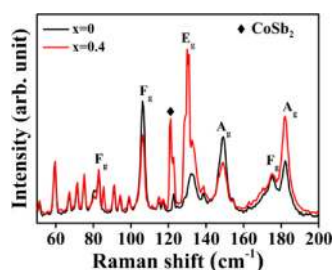


Fig. 5. The Raman spectra of  $(\text{InSb})_x + \text{Yb}_{0.2}\text{Co}_4\text{Sb}_{12}$  taken with a laser of wavelength 532 nm.

Table 2  
Peak positions of the Raman active modes.

$\text{Yb}_{0.2}\text{Co}_4\text{Sb}_{12}$ ( $\text{cm}^{-1}$ )	$(\text{InSb})_{0.4}$ + $\text{Yb}_{0.2}\text{Co}_4\text{Sb}_{12}$ ( $\text{cm}^{-1}$ )	$\text{Co}_4\text{Sb}_{12}$ [35] ( $\text{cm}^{-1}$ )	Raman active mode
59	59	60	$F_u$
83	83	82	$F_g$
106	106	109	$F_g$
123	121	–	$\text{CoSb}_2$
132	130	135	$E_g$
149	149	152	$A_g$
175	177	178	$F_g$
182	182	186	$A_g$

(Fig. 6). The increase of  $\rho(T)$  above the Debye temperature ( $\theta_D$ ) [ $\theta_D = 307$  K for  $\text{Yb}_{0.2}\text{Co}_4\text{Sb}_{12}$  [40]] is mainly due to the charge carrier-phonon scattering, which leads to a reduction of charge carrier mobility ( $\mu$ ). From the equation:  $1/\rho = ne\mu$ ,  $\rho(T)$  is inversely proportional to  $\mu$ ;  $n$  is the charge carrier concentration and  $e$  the electronic charge. Hence, the reduction of  $\mu$  resulted in an increase in  $\rho(T)$ . The small negative curvature above 650 K is likely due to the  $s$ - $d$  scattering of conduction electrons [41].  $\text{Yb}_{0.2}\text{Co}_4\text{Sb}_{12}$  exhibited a lower electrical resistivity than  $\text{Co}_4\text{Sb}_{12}$ . The electropositive Yb with a valence state of +3 in the voids of  $\text{Co}_4\text{Sb}_{12}$ , confirmed from XPS analysis [see Supplementary Material, Section 4], provides 3 electrons to  $\text{Co}_4\text{Sb}_{12}$  per Yb atom, which leads to an increased charge carrier density and a lower electrical resistivity of  $\text{Yb}_{0.2}\text{Co}_4\text{Sb}_{12}$  ( $6.67 \mu\Omega\text{-m}$  at 300 K) than that of pure  $\text{Co}_4\text{Sb}_{12}$  ( $300 \mu\Omega\text{-m}$  at 300 K [7]). A similar value of electrical resistivity was reported by Nolas et al. ( $6.17 \mu\Omega\text{-m}$  at 300 K for  $\text{Yb}_{0.19}\text{Co}_4\text{Sb}_{12}$  [20]) and Yang et al. ( $6.10 \mu\Omega\text{-m}$  at 300 K for  $\text{Yb}_{0.19}\text{Co}_4\text{Sb}_{12}$  [22]). A systematic increase in  $\rho(T)$  was expected after the addition of InSb in the matrix due to increased scattering of charge carriers at the interfaces induced by InSb nano inclusions. But the presence of multiple secondary phases of different sizes ( $\text{CoSb}_2$ ,  $\text{Yb}_2\text{O}_3$ ) in addition to the InSb phase influenced the charge carrier transport differently. The composite with  $x = 0.1$  and  $0.3$  exhibited a higher  $\rho(T)$  value than the matrix, whereas a decrease in  $\rho(T)$  was observed for the composite with  $x = 0.2$  and  $0.4$ . To understand this anomalous behavior of composites, the charge carrier concentration of the composites was estimated from Hall measurements at room temperature. A carrier concentration lower than that of the matrix was found for the composite with

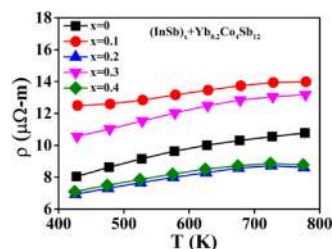


Fig. 6. Temperature dependence of electrical resistivity ( $\rho$ ) of  $(\text{InSb})_x + \text{Yb}_{0.2}\text{Co}_4\text{Sb}_{12}$  (where  $x = 0, 0.1, 0.2, 0.3, 0.4$ ) in the temperature range: 423–773 K.

Table 3  
Charge carrier concentration ( $n$ ) of  $(\text{InSb})_x + \text{Yb}_{0.2}\text{Co}_4\text{Sb}_{12}$  at room temperature (obtained from respective Hall data).

Sample	Carrier concentration ( $n$ ) $\times 10^{20}$ ( $\text{cm}^{-3}$ )
$x = 0$	2.66
$x = 0.1$	1.65
$x = 0.2$	2.86
$x = 0.3$	1.73
$x = 0.4$	2.72

$x = 0.1$  and  $0.3$ , in contrast to the composite with  $x = 0.2$  and  $0.4$  with a slight increase in the carrier concentration (see Table 3). Hence, the trends of the carrier concentration control the trends of the electrical resistivity. The different carrier concentrations in the composites can be attributed to the different content of secondary phases present in the composites. A higher amount of  $\text{Yb}_2\text{O}_3$  oxide phase was detected for the composite with  $x = 0.1$  and  $0.3$  compared to other samples (see Table 1), which enhanced the electrical resistivity in these two composites. Then again,  $\text{CoSb}_2$  ( $3.4 \mu\Omega\text{-m}$  at 300 K [42]) and InSb ( $\sim 18 \mu\Omega\text{-m}$  at 300 K [43]) are metallic phases with lower electrical resistivity. They can also influence the overall electrical resistivity of composites. In addition, the interfaces of matrix and secondary phases of a wide size range can scatter the charge carriers and alter the electrical resistivity. From the variation of the electrical resistivity, it is clear that the  $\text{Yb}_2\text{O}_3$  oxide impurity phases have a more pronounced effect on the carrier transport than other phases. Previous studies have also reported an enormous impact of the small amount of  $\text{Yb}_2\text{O}_3$  oxide impurities on the electrical resistivity of the materials [44]. The difference in density of the composites (see Table 1) can affect the electrical resistivity too. In conclusion, along with the InSb inclusion phase, other secondary phases present in the composites also significantly impact the charge carrier transport and the electrical resistivity.

#### 3.4.2. Seebeck coefficient ( $S$ )

Fig. 7 shows the Seebeck coefficient variation as a function of temperature,  $S(T)$ , of  $(\text{InSb})_x + \text{Yb}_{0.2}\text{Co}_4\text{Sb}_{12}$  composites. All the composites exhibited a negative  $S(T)$ , indicating electrons as the majority charge carriers stemming from the charge carrier transfer from Yb to  $\text{Co}_4\text{Sb}_{12}$  [20–22]. The Mott formula gives  $S(T)$  at an absolute temperature  $T$  for a degenerate semiconducting material:

$$S = \frac{\pi^2 k_B^2 T}{3} \left[ \frac{1}{n} \frac{dn}{dT} + \frac{1}{\mu} \frac{d\mu}{dT} \right]_{E=E_F} \quad (1)$$

where  $n$  is the carrier concentration,  $k_B$  is Boltzmann's constant, and  $\mu$  is the charge carrier mobility.  $S(T)$  increased linearly with increasing temperature, then saturated at around 680 K, and decreased beyond 700 K. The decrease in  $\mu$  due to scattering of charge carriers by thermally excited phonons led to an increase in  $S(T)$  with temperature for all the composites. According to Eq. (1), as  $S(T)$  is dependent on both the temperature-dependent parameters,  $n$  and  $\mu$ , a

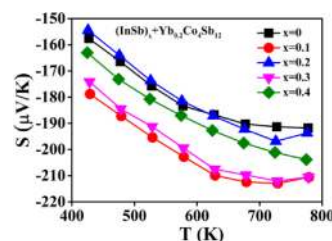


Fig. 7. Temperature dependence of the Seebeck coefficient of  $(\text{InSb})_x + \text{Yb}_{0.2}\text{Co}_4\text{Sb}_{12}$  ( $x = 0, 0.1, 0.2, 0.3, 0.4$ ).

non-linear behavior of  $S(T)$  can be expected at a higher temperature. The decrease in  $S(T)$  above 700 K could also be due to the activation of minority charge carriers.  $S(T)$  was observed to increase for the composites with  $x = 0.1$  and  $0.3$ , which can be attributed to the decreased charge carrier concentration in these two composites (Table 3). The other two composites ( $x = 0.2$  and  $0.4$ ) and  $\text{Yb}_{0.2}\text{Co}_4\text{Sb}_{12}$  showed nearly similar  $S(T)$  values due to the similar carrier concentration in these samples. The filtering of low energy charge carriers at the interfaces between secondary phases and  $\text{Yb}_{0.2}\text{Co}_4\text{Sb}_{12}$  can also enhance the absolute  $S(T)$  values of composites [45,46].  $S(T)$  did not follow any systematic trend with increasing InSb content, similar to  $\rho(T)$  due to the irregular distribution of different amounts of secondary phases of  $\text{Yb}_2\text{O}_3$ ,  $\text{CoSb}_2$ , and InSb in the composites.

### 3.4.3. Thermal conductivity

Fig. 8(a) shows the temperature dependence of the total thermal conductivity,  $\kappa$ , of  $(\text{InSb})_x + \text{Yb}_{0.2}\text{Co}_4\text{Sb}_{12}$  composites. The Wiedemann-Franz relation:  $\kappa_e = LT/\rho$  was used to determine the electronic contribution to the thermal conductivity ( $\kappa_e$ ), where  $L$  is the temperature-dependent Lorenz number [see Supplementary Material, Section 5],  $T$  the absolute temperature and  $\rho$  the electrical resistivity. The detailed calculation of  $L$  is explained in Ref [47].  $\kappa_e$  is plotted in Fig. 8(b). The lattice contribution,  $\kappa_L$ , to the thermal conductivity was extracted by deducting  $\kappa_e$  from  $\kappa$  ( $\kappa_L = \kappa - \kappa_e$ ) and is plotted in Fig. 8(c).

$\kappa$  of all composites was almost independent of temperature in the whole measured temperature range.  $\kappa_e$  increased with increasing temperature, whereas  $\kappa_L$  showed a weak temperature dependence. The lower  $\kappa_L$  of  $\text{Yb}_{0.2}\text{Co}_4\text{Sb}_{12}$ , as compared to pure  $\text{Co}_4\text{Sb}_{12}$  [7.5 W/mK [7]], is due to the rattling of Yb-fillers in the voids, having large atomic displacement parameters [48]. It was found that Yb rattles inside the void with a frequency of  $43 \text{ cm}^{-1}$  and scatters the phonons with similar frequency [49]. The rattling of Yb produced anharmonicity in the system and reduced  $\kappa_L$  significantly, reported by previous groups, as well [20,21,33]. In the nanocomposites, the phonons with a mean free path large or similar to the grain interface spacing get scattered at the interfaces [50]. The distribution of  $\text{Yb}_2\text{O}_3$  at the grain boundaries also decreased  $\kappa_L$  compared to pure  $\text{Co}_4\text{Sb}_{12}$ , by interface phonon scattering. It can be seen that  $\kappa$  decreased in all the composites compared to that of  $\text{Yb}_{0.2}\text{Co}_4\text{Sb}_{12}$ , mainly due to the decrease in  $\kappa_L$  by the addition of InSb. The reduction in  $\kappa_L$  can be attributed to the scattering of phonons at the interfaces of  $\text{CoSb}_2$ ,

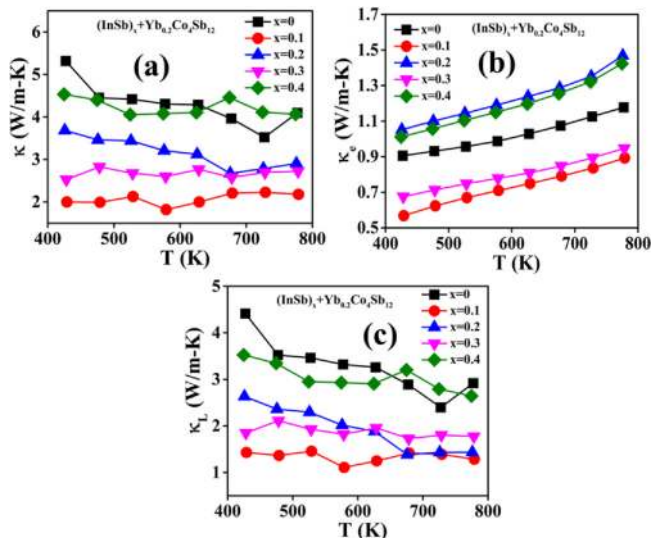


Fig. 8. Temperature dependence of (a) total thermal conductivity ( $\kappa$ ), (b) electronic thermal conductivity ( $\kappa_e$ ) and (c) lattice thermal conductivity ( $\kappa_L$ ) of  $(\text{InSb})_x + \text{Yb}_{0.2}\text{Co}_4\text{Sb}_{12}$  ( $x = 0, 0.1, 0.2, 0.3, 0.4$ ).

InSb,  $\text{Yb}_2\text{O}_3$ , and  $\text{Yb}_{0.2}\text{Co}_4\text{Sb}_{12}$ . The main contribution to the lattice part of the thermal conductivity stems from the long-wavelength acoustic phonons with a mean free path of 10–100 nm [51]. From microstructural analysis, InSb grains of 20–200 nm were found to be dispersed in bulk  $\text{Yb}_{0.2}\text{Co}_4\text{Sb}_{12}$  matrix. Hence, the phonons with similar mean free paths were scattered at the interfaces of nanosized InSb second phase and  $\text{Yb}_{0.2}\text{Co}_4\text{Sb}_{12}$  matrix phase. The composite with the lowest InSb content ( $x = 0.1$ ) showed the lowest  $\kappa_L$  value (1.8–2.2 W/m-K for the temperature range of 423–773 K). However, an increase in  $\kappa_L$  with increasing InSb content was observed. Ghosh et al. [52] also demonstrated a systematic increase in  $\kappa_L$  of  $(\text{InSb})_x + \text{Ba}_{0.3}\text{Co}_4\text{Sb}_{12}$  composites with increasing InSb content. This is because the InSb inclusion phase is highly thermally conductive ( $\kappa = 14 \text{ W/m-K}$  at room temperature [43]), and hence contributed to the overall increase in the lattice thermal conductivity of composites. Also, the amount of  $\text{Yb}_2\text{O}_3$  was higher in the composites with  $x = 0.1$  and  $0.3$ . It can contribute to the lower lattice thermal conductivity of the composites as well. In summary, these two combined effects of filling and nanocomposite approaches reduced the lattice thermal conductivity significantly.

### 3.4.4. Power factor (P.F. = $S^2/\rho$ ) and figure of merit (zT)

Fig. 9(a) shows the power factor (P.F.) of  $(\text{InSb})_x + \text{Yb}_{0.2}\text{Co}_4\text{Sb}_{12}$  composites as a function of temperature. A maximum P.F. of  $3.51 \text{ mW/mK}^2$  at 673 K was achieved for  $\text{Yb}_{0.2}\text{Co}_4\text{Sb}_{12}$ . Yang et al. theoretically predicted a maximum P.F. of  $\sim 3.50 \text{ mW/mK}^2$  at 800 K for  $\text{Yb}_{0.25}\text{Co}_4\text{Sb}_{12}$ , which agrees well with our study [53]. The composites with  $x = 0.2$  and  $0.4$  exhibited an increase in P.F. compared to that of  $\text{Yb}_{0.2}\text{Co}_4\text{Sb}_{12}$ . A maximum P.F. value of  $4.73 \text{ mW/mK}^2$  at 773 K was achieved for the composite with  $x = 0.4$  due to the lowest  $\rho(T)$  of this composite. Although  $S(T)$  is enhanced in the  $x = 0.1$  and  $0.3$  composites compared to the matrix, these two composites exhibited P.F. similar to the matrix due to the high  $\rho(T)$  values. The figure of merit (zT) of the composites was calculated as a function of temperature and is displayed in Fig. 9(b). An increase in zT was observed with increasing temperature up to 723 K and then saturated. The zT of  $\text{Yb}_{0.2}\text{Co}_4\text{Sb}_{12}$  reached a maximum value of 0.72 at 723 K. The zT values achieved by Nolas et al. [20] (zT  $\sim 1$  at 600 K for  $\text{Yb}_{0.19}\text{Co}_4\text{Sb}_{12}$ ), Ryll et al. [21] (zT  $\sim 1.0$  at 723 K for  $\text{Yb}_{0.25}\text{Co}_4\text{Sb}_{12}$ ), and Yang et al. [22] (zT  $\sim 1.2$  at 823 K for  $\text{Yb}_{0.35}\text{Co}_4\text{Sb}_{12}$ ) are higher than our achieved zT. All the composites showed a higher zT than the matrix. A systemic increase in  $\kappa$  with increasing InSb content resulted in a systematic decrease in the zT value with increasing InSb content in the composites. The lower total thermal conductivity of the composites with  $x = 0.1$  and  $x = 0.2$  yielded a maximum zT of  $\sim 1.2$  at 773 K with an average zT of  $\sim 0.90$  for the temperature range of 423–773 K. This zT is comparable with the reported zTs of nanocomposites of Yb-filled  $\text{Co}_4\text{Sb}_{12}$  such as zT = 1.3 at 850 K for  $\text{Yb}_{0.25}\text{Co}_4\text{Sb}_{12}/\text{Yb}_2\text{O}_3$  [54], zT = 0.95 at 700 K for  $\text{Yb}_{0.15}\text{Co}_4\text{Sb}_{12}/\text{CoSb}_3$  [55] and zT = 1 at 603 K for  $\text{Ag}/\text{Yb}_{0.35}\text{Co}_4\text{Sb}_{12}$  [14]. In conclusion, the distribution of InSb nano inclusions in the matrix of Yb-filled  $\text{Co}_4\text{Sb}_{12}$  reduced the lattice contribution to the thermal conductivity significantly and, as a result, enhanced the thermoelectric figure of merit.

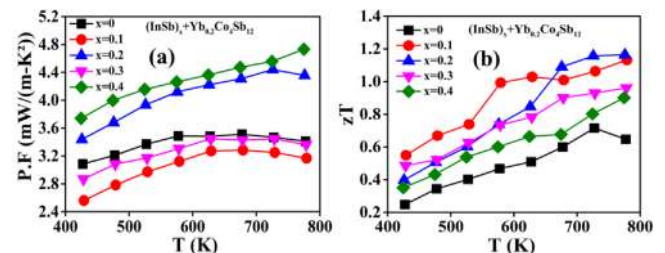


Fig. 9. Temperature dependence of (a) power factor and (b) figure of merit (zT) of  $(\text{InSb})_x + \text{Yb}_{0.2}\text{Co}_4\text{Sb}_{12}$  ( $x = 0, 0.1, 0.2, 0.3, 0.4$ ).

The thermoelectric efficiency of the composites was estimated using the equation:

$$\eta = \frac{T_h - T_c}{T_h} \frac{\sqrt{1 + (zT)_a} - 1}{\sqrt{1 + (zT)_a} + \frac{T_c}{T_h}} \quad (2)$$

where  $\frac{T_h - T_c}{T_h}$  is the Carnot efficiency,  $T_h$  is the temperature of the hot side, and  $T_c$  is the temperature of the cold side.  $(zT)_a$  is the average  $zT$  of the material for the temperature range of 423–773 K. The highest thermal-to-electric efficiency of 8.89% for  $x=0.1\%$  and 8.28% for  $x=0.2$  were achieved.

#### 4. Conclusions

The nanocomposites of  $\text{Yb}_{0.2}\text{Co}_4\text{Sb}_{12}$  and  $\text{InSb}$  were synthesized using high-energy ball milling and spark plasma sintering. The thermoelectric properties of these composites were investigated in the temperature range of 423–773 K. Impurity phases of  $\text{CoSb}_2$  and  $\text{Yb}_2\text{O}_3$  were found in the matrix. In composites, both the  $\text{InSb}$  inclusion phase and  $\text{Yb}_2\text{O}_3$  impurity phases were found situated at the grain boundaries of  $\text{Yb}_{0.2}\text{Co}_4\text{Sb}_{12}$ . Additionally, the nanocrystalline  $\text{InSb}$  grains (20–200 nm) were homogeneously distributed within the matrix grains.  $\text{Yb}$  filler in  $\text{Co}_4\text{Sb}_{12}$  with a valence state of +3 resulted in a low electrical resistivity value. The variation in the electrical resistivity and the Seebeck coefficient was not systematic with increasing  $\text{InSb}$  content. The presence of multiple secondary phases ( $\text{InSb}$ ,  $\text{Yb}_2\text{O}_3$ ,  $\text{CoSb}_2$ ) with grains of a broad size range in the composites influenced the charge carrier transport differently. The reduction in total thermal conductivity of the composites was due to the anharmonicity in the system originating from rattling of the  $\text{Yb}$ -filler in the voids in combination with the scattering of phonons at the interfaces of matrix and secondary phases. It was found that  $\text{Yb}_2\text{O}_3$  oxide impurity mainly influences the charge carrier transport, whereas the nanocrystalline  $\text{InSb}$  phase mainly influences the heat transport of phonons. The highest  $zT$  of  $\sim 1.2$  at 773 K was achieved for the  $(\text{InSb})_{0.1} + \text{Yb}_{0.2}\text{Co}_4\text{Sb}_{12}$  and  $(\text{InSb})_{0.2} + \text{Yb}_{0.2}\text{Co}_4\text{Sb}_{12}$  composites with a thermoelectric efficiency of 8.89% and 8.28%, respectively.

#### CRedit authorship contribution statement

S.G. synthesized the materials, performed XRD, EPMA, XPS, Raman characterization, Hall measurement, measured the Seebeck coefficient and electrical resistivity, analyzed the data and wrote the manuscript. S.T. performed DSC measurement and analyzed the data. G.S. and S.S. performed EBSD experiment and helped with the analysis. A.K. and B.S.M. carried out SPS sintering. G.R., P.R. and E.B. helped with the high temperature thermal conductivity measurement and analysis. S.R.K.M. performed TEM experiment. R.C.M. defined the project and gave technical inputs related to synthesis, structural characterization and interpretation and analysis of the data. All authors helped in the preparation of the manuscript.

#### Declaration of Competing Interest

The authors declare that they have no known competing financial interests or personal relationships that could have appeared to influence the work reported in this paper.

#### Acknowledgments

The authors would like to thank the Indo-Austria joint project IN06, funded by DST (grant no: INT/AUSTRIA/BMWF/P-06/2018) and the Austrian OeAD (Project: IN 02/2018). The authors would also like to acknowledge the University Grants Commission (grant no: F.530/26/CAS-VI/2018(SAP-I)), India, for the DSC instrument.

#### Appendix A. Supporting information

Supplementary data associated with this article can be found in the online version at doi:10.1016/j.jallcom.2021.160532.

#### References

- [1] C. Uher, Chapter 5 Skutterudites: prospective novel thermoelectrics, in: T.M. Tritt (Ed.), *Semiconductors and semimetals*, Vol. 69 Elsevier, Academic Press, San Diego, 2001, pp. 139–253.
- [2] G. Rogl, P. Rogl, Skutterudites, a most promising group of thermoelectric materials, *Curr. Opin. Green. Sustain. Chem.* 4 (2017) 50–57.
- [3] D.J. Singh, W.E. Pickett, Skutterudite antimonides: quasilinear bands and unusual transport, *Phys. Rev. B* 50 (1994) 11235–11238.
- [4] M. Rull-Bravo, A. Moure, J.F. Fernández, M. Martín-González, Skutterudites as thermoelectric materials: Revisited, *RSC Adv.* 5 (2015) 41653–41667.
- [5] J.P. Fleurial, T. Caillat, A. Borshchevsky, Skutterudites: an update, in: XVI ICT'97. Proceedings ICT'97. 16th International Conference on Thermoelectrics (Cat. No. 97TH8291).
- [6] Y. Tang, Z.M. Gibbs, L.A. Agapito, G. Li, H.S. Kim, M.B. Nardelli, S. Curtarolo, G.J. Snyder, Convergence of multi-valley bands as the electronic origin of high thermoelectric performance in  $\text{CoSb}_3$  skutterudites, *Nat. Mater.* 14 (2015) 1223–1228.
- [7] Y. Kawaharada, K. Kurosaki, M. Uno, S. Yamanaka, Thermoelectric properties of  $\text{CoSb}_3$ , *J. Alloy. Compd.* 315 (2001) 193–197.
- [8] G.A. Slack, V.G. Tsoukala, Some properties of semiconducting  $\text{IrSb}_3$ , *J. Appl. Phys.* 76 (1994) 1665–1671.
- [9] F. Chen, R. Liu, Z. Yao, Y. Xing, S. Bai, L. Chen, Scanning laser melting for rapid and massive fabrication of filled skutterudites with high thermoelectric performance, *J. Mater. Chem. A* 6 (2018) 6772–6779.
- [10] M. Benyahia, V. Ohorodniichuk, E. Leroy, A. Dauscher, B. Lenoir, E. Alleno, High thermoelectric figure of merit in mesostructured  $\text{In}_{0.25}\text{Co}_4\text{Sb}_{12}$  n-type skutterudite, *J. Alloy. Compd.* 735 (2018) 1096–1104.
- [11] G. Rogl, A. Grytsiv, K. Yubuta, S. Puchegger, E. Bauer, C. Raju, R.C. Mallik, P. Rogl, In-doped multifilled n-type skutterudites with  $ZT = 1.8$ , *Acta Mater.* 95 (2015) 201–211.
- [12] Y. Li, P. Qiu, H. Duan, J. Chen, G.J. Snyder, X. Shi, B.B. Iversen, L. Chen, Enhanced thermoelectric performance in rare-earth filled-skutterudites, *J. Mater. Chem. C* 4 (2016) 4374–4379.
- [13] P. Wen, H. Yang, X. Zhou, B. Duan, P. Zhai, Enhanced thermoelectric figure of merit of  $\text{Co}_4\text{Sb}_{11.5}\text{Te}_{0.5}$  via a two-pronged strategy combining grain refinement and nano-inclusions, *Mater. Lett.* 223 (2018) 190–193.
- [14] P. Chen, Z. Zhou, W. Jiang, W. Luo, J. Yang, J. Zhu, L. Wang, Y. Fan, Enhancing the thermoelectric performance of filled skutterudite nanocomposites in a wide temperature range via electroless silver plating, *Scr. Mater.* 146 (2018) 136–141.
- [15] H. Li, X. Su, X. Tang, Q. Zhang, C. Uher, G.J. Snyder, U. Aydemir, Grain boundary engineering with nano-scale  $\text{InSb}$  producing high performance  $\text{In}_x\text{Ce}_y\text{Co}_4\text{Sb}_{12+z}$  skutterudite thermoelectrics, *J. Mater.* 3 (2017) 273–279.
- [16] S. Ghosh, A. Bisht, A. Karati, G. Rogl, P.F. Rogl, B.S. Murty, S. Suwas, R.C. Mallik, Thermoelectric properties of  $\text{Co}_4\text{Sb}_{12}$  with  $\text{Bi}_2\text{Te}_3$  nanoinclusions, *J. Phys. Condens. Matter.* 30 (2018) 095701.
- [17] A. Moure, M. Rull-bravo, B. Abad, A.D. Campo, M. Muñoz, M.H. Aguirre, A. Jacquot, J.F. Fernandez, M. Martin-gonzalez, Thermoelectric Skutterudite/oxide nanocomposites: effective decoupling of electrical and thermal conductivity by functional interfaces, *Nano Energy* 31 (2017) 393–402.
- [18] G. Rogl, P. Rogl, How nanoparticles can change the figure of merit,  $ZT$ , and mechanical properties of skutterudites, *Mater. Today Phys.* 3 (2017) 48–69.
- [19] X. Shi, J. Yang, J.R. Salvador, M. Chi, J.Y. Cho, H. Wang, S. Bai, J. Yang, W. Zhang, L. Chen, Multiple-filled skutterudites: high thermoelectric figure of merit through separately optimizing electrical and thermal transports, *J. Am. Chem. Soc.* 133 (2011) 7837–7846.
- [20] G.S. Nolas, M. Kaeser, R.T. Littleton IV, T.M. Tritt, High figure of merit in partially filled ytterbium skutterudite materials, *Appl. Phys. Lett.* 77 (2000) 1855–1857.
- [21] B. Ryll, A. Schmitz, J.D. Boor, A. Franz, P.S. Whitfield, M. Reehuis, A. Hoser, E. Müller, K. Habicht, K. Fritsch, Structure, phase composition, and thermoelectric properties of  $\text{Yb}_x\text{Co}_4\text{Sb}_{12}$  and their dependence on synthesis method, *ACS Appl. Energy Mater.* 1 (2018) 113–122.
- [22] J. Yang, Q. Hao, H. Wang, Y.C. Lan, Q.Y. He, A. Minnich, D.Z. Wang, J. Harriman, V.M. Varkki, M.S. Dresselhaus, G. Chen, Z.F. Ren, Solubility study of  $\text{Yb}$  in n-type skutterudites  $\text{Yb}_x\text{Co}_4\text{Sb}_{12}$  and their enhanced thermoelectric properties, *Phys. Rev. B* 80 (2009) 115329.
- [23] J. Peng, X. Liu, L. Fu, W. Xu, Q. Liu, J. Yang, Synthesis and thermoelectric properties of  $\text{In}_{0.2+x}\text{Co}_4\text{Sb}_{12+x}$  composite, *J. Alloy. Compd.* 521 (2012) 141–145.
- [24] H. Li, X. Su, X. Tang, Q. Zhang, C. Uher, G.J. Snyder, U. Aydemir, Grain boundary engineering with nano-scale  $\text{InSb}$  producing high performance  $\text{In}_x\text{Ce}_y\text{Co}_4\text{Sb}_{12+z}$  skutterudite thermoelectrics, *J. Mater.* 3 (2017) 273–279.
- [25] H. Li, X. Tang, Q. Zhang, C. Uher, High performance  $\text{In}_x\text{Ce}_y\text{Co}_4\text{Sb}_{12}$  thermoelectric materials with in situ forming nanostructured  $\text{InSb}$  phase, *Appl. Phys. Lett.* 94 (2009) 102114.
- [26] A. Gharleghi, P.C. Hung, F.H. Lin, C.J. Liu, Enhanced  $ZT$  of  $\text{In}_x\text{Co}_4\text{Sb}_{12}$ - $\text{InSb}$  nanocomposites fabricated by hydrothermal synthesis combined with solid-vapor reaction: a signature of phonon-glass and electron-crystal materials, *ACS Appl. Mater. Interfaces* 8 (2016) 35123–35131.
- [27] X. Shi, W. Zhang, L.D. Chen, J. Yang, Filling fraction limit for intrinsic voids in crystals: doping in skutterudites, *Phys. Rev. Lett.* 95 (2005) 185503.

- [28] X. Shi, W. Zhang, L.D. Chen, J. Yang, C. Uher, Thermodynamic analysis of the filling fraction limits for impurities in  $\text{CoSb}_3$  based on ab initio calculations, *Acta Mater.* 56 (2008) 1733–1740.
- [29] Z.G. Mei, W. Zhang, L.D. Chen, J. Yang, Filling fraction limits for rare-earth atoms in  $\text{CoSb}_3$ : an ab initio approach, *Phys. Rev. B* 74 (2006) 153202.
- [30] S. Ghosh, S.M. Valiyaveetil, G. Shankar, T. Maity, K.H. Chen, K. Biswas, S. Suwas, R.C. Mallik, Enhanced Thermoelectric Properties of In-filled  $\text{Co}_4\text{Sb}_{12}$  with InSb Nanoinclusions, *ACS Appl. Energy Mater.* 3 (2019) 635–646.
- [31] J. Rodriguez-Carvajal, FULLPROF: a program for Rietveld refinement and pattern matching analysis, in: *Satellite Meeting on Powder Diffraction of the XV Congress of the IUCr*, 1990, p.127.
- [32] J. Nagao, D. Nataraj, M. Ferhat, T. Uchida, S. Takeya, T. Ebinuma, H. Anno, K. Matsubara, E. Hatta, K. Mukasa, Phonon behaviors and electronic structures of the filled skutterudite  $\text{Yb}_y\text{Co}_4\text{Sb}_{12}$  compounds: an electron tunneling study, *J. Appl. Phys.* 92 (2002) 4135–4137.
- [33] Y. Tang, S.W. Chen, G.J. Snyder, Temperature dependent solubility of Yb in  $\text{Yb-CoSb}_3$  skutterudite and its effect on preparation, optimization and lifetime of thermoelectrics, *J. Mater.* 1 (2015) 75–84.
- [34] Y. Li, X. Shi, D. Ren, J. Chen, L. Chen, Investigation of the anisotropic thermoelectric properties of oriented polycrystalline  $\text{SnSe}$ , *Energies* 8 (2015) 6275–6285.
- [35] G.S. Nolas, C.A. Kendziora, Raman spectroscopy investigation of lanthanide-filled and unfilled skutterudites, *Phys. Rev. B* 59 (1999) 6189–6192.
- [36] G. Rogl, A. Grytsiv, J. Bursik, J. Horky, R. Anbalagan, E. Bauer, R.C. Mallik, P. Rogl, M. Zehetbauer, Changes in microstructure and physical properties of skutterudites after severe plastic deformation, *Phys. Chem. Chem. Phys.* 17 (2015) 3715–3722.
- [37] M. Rotter, P. Rogl, A. Grytsiv, W. Wolf, M. Krisch, A. Mirone, Lattice dynamics of skutterudites: inelastic x-ray scattering on  $\text{CoSb}_3$ , *Phys. Rev. B* 77 (2008) 144301.
- [38] L.X. Li, H. Liu, J.Y. Wang, X.B. Hu, S.R. Zhao, H.D. Jiang, Q.J. Huang, H.H. Wang, Z.F. Li, Raman spectroscopy investigation of partially filled skutterudite, *Chem. Phys. Lett.* 347 (2001) 373–377.
- [39] P. Lu, Z. Shen, X. Hu, Effects of the voids filling on the lattice vibrations for the  $\text{CoSb}_3$ -based thermoelectric materials-Raman scattering spectra and theoretical study, *Phys. B Condens. Matter* 405 (2010) 2589–2592.
- [40] I.K. Dimitrov, M.E. Manley, S.M. Shapiro, J. Yang, W. Zhang, L.D. Chen, Q. Jie, G. Ehlers, A. Podlesnyak, J. Camacho, Q. Li, Einstein modes in the phonon density of states of the single-filled skutterudite  $\text{Yb}_{0.2}\text{Co}_4\text{Sb}_{12}$ , *Phys. Rev. B* 82 (2010) 174301.
- [41] N.F. Mott, The electrical conductivity of transition metals, in: *Proceedings of the Royal Society of London. Series A-Mathematical and Physical Sciences*, 153, 1936, pp. 699–717.
- [42] T. Caillat, Preparation and thermoelectric properties of  $\text{Ir}_x\text{Co}_{1-x}\text{Sb}_2$  alloys, *J. Phys. Chem. Solids* 57 (1996) 1351–1358.
- [43] Y. Cheng, J. Yang, Q. Jiang, D. He, J. He, Y. Luo, D. Zhang, Z. Zhou, Y. Ren, J. Xin, New insight into InSb-based thermoelectric materials: from a divorced eutectic design to a remarkably high thermoelectric performance, *J. Mater. Chem. A* 5 (2017) 5163–5170.
- [44] K.P. Devlin, J.H. Grebenkemper, K. Lee, G. Cerretti, S.K. Bux, S.M. Kauzlarich, Enhancement of the thermal stability and thermoelectric properties of  $\text{Yb}_{1.4}\text{MnSb}_{11}$  by Ce substitution, *Chem. Mater.* 32 (2020) 9268–9276.
- [45] J.P. Heremans, C.M. Thrush, D.T. Morelli, Thermopower enhancement in lead telluride nanostructures, *Phys. Rev. B* 70 (2004) 115334.
- [46] A. Pakdel, Q. Guo, V. Nicolosi, T. Mori, Enhanced thermoelectric performance of Bi-Sb-Te/Sb<sub>2</sub>O<sub>3</sub> nanocomposites by energy filtering effect, *J. Mater. Chem. A* 6 (2018) 21341–21349.
- [47] D.M. Rowe, C.M. Bhandari, *Modern Thermoelectrics*, (Virginia), 1983.
- [48] S.Q. Bai, X.Y. Huang, L.D. Chen, W. Zhang, X.Y. Zhao, Y.F. Zhou, Thermoelectric properties of n-type  $\text{Sr}_x\text{M}_y\text{Co}_4\text{Sb}_{12}$  (M = Yb, Ba) double-filled skutterudites, *Appl. Phys. A* 100 (2010) 1109–1114.
- [49] J. Yang, W. Zhang, S.Q. Bai, Z. Mei, L.D. Chen, Dual-frequency resonant phonon scattering in  $\text{Ba}_x\text{R}_y\text{Co}_4\text{Sb}_{12}$  (R=La,Ce, and Sr), *Appl. Phys. Lett.* 90 (2007) 192111.
- [50] M. Zebarjadi, J. Yang, K. Lukas, B. Kozinsky, B. Yu, M.S. Dresselhaus, C. Opeil, Z. Ren, G. Chen, Role of phonon dispersion in studying phonon mean free paths in skutterudites, *J. Appl. Phys.* 112 (2012) 044305.
- [51] W. Kim, R. Wang, A. Majumdar, Nanostructuring expands thermal limits, *Nano Today* 2 (2007) 40–47.
- [52] S. Ghosh, G. Shankar, A. Karati, K. Werbach, G. Rogl, P. Rogl, E. Bauer, B.S. Murty, S. Suwas, R.C. Mallik, Enhanced thermoelectric performance in the  $\text{Ba}_{0.3}\text{Co}_4\text{Sb}_{12}/\text{InSb}$  nanocomposite originating from the minimum possible lattice thermal conductivity, *ACS Appl. Mater. Interfaces* 12 (2020) 48729–48740.
- [53] J. Yang, L. Xi, W. Zhang, L.D. Chen, J. Yang, Electrical transport properties of filled  $\text{CoSb}_3$  skutterudites: a theoretical study, *J. Electron. Mater.* 38 (2009) 1397–1401.
- [54] X.Y. Zhao, X. Shi, L.D. Chen, W.Q. Zhang, S.Q. Bai, Y.Z. Pei, X.Y. Li, T. Goto, Synthesis of  $\text{Yb}_y\text{Co}_4\text{Sb}_{12}/\text{Yb}_2\text{O}_3$  composites and their thermoelectric properties, *Appl. Phys. Lett.* 89 (2006) 092121.
- [55] J.L. Mi, X.B. Zhao, T.J. Zhu, J.P. Tu, Thermoelectric properties of  $\text{Yb}_{0.15}\text{Co}_4\text{Sb}_{12}$  based nanocomposites with  $\text{CoSb}_3$  nano-inclusion, *J. Phys. D Appl. Phys.* 41 (2008) 205403.